SCIENCE CHINA
Physics, Mechanics & Astronomy

• Article •

March 2026 Vol. 69 No. 3: 236111
https://doi.org/10.1007/s11433-025-2845-y

A highly efficient amorphous catalyst achieved by ultrasonic vibration

Jiayi Ruan[1†], Wei Li[1†], Chenchen Yuan[1*], Luyao Li[1,2], Weihang Feng[1], Wei He[1], Tao Lu[1], Fujun Lan[3,4,5], Qiaoshi Zeng[3,4], Yujiao Lu[6], Zheng Wang[6], Xuelian Wu[7], Yubing Ke[8*], Hua Yang[8], Jiang Ma[2*], Ye Pan[1], and Weihua Wang[9,10]

[1] *School of Materials Science and Engineering, Jiangsu Key Laboratory for Advanced Metallic Materials, Southeast University, Nanjing 211189, China*

[2] *Shenzhen Key Laboratory of High Performance Nontraditional Manufacturing, College of Mechatronics and Control Engineering, Shenzhen University, Shenzhen 518060, China*

[3] *Center for High Pressure Science and Technology Advanced Research, Shanghai 201203, China*

[4] *Shanghai Key Laboratory of Material Frontiers Research in Extreme Environments (MFree), Institute for Shanghai Advanced Research in Physical Sciences (SHARPS), Shanghai 201203, China*

[5] *Shanghai Institute of Laser Plasma, Shanghai 201203, China*

[6] *Key Laboratory for Liquid-Solid Structural Evolution and Processing of Materials (Ministry of Education), Shandong University, Jinan 250061, China*

[7] *Advanced Ceramics Research Center, School of Materials Science and Engineering, Anhui University of Technology, Ma'anshan 243032, China*

[8] *China Spallation Neutron Source, Dongguan Branch, Institute of High Energy Physics, Chinese Academy of Sciences, Dongguan 523803, China*

[9] *Institute of Physics, Chinese Academy of Sciences, Beijing 100190, China*

[10] *Songshan Lake Materials Laboratory, Dongguan 523808, China*

Received September 3, 2025; accepted October 30, 2025; published online January 15, 2026

The growing usage of industrial dyes makes the sewage treatment a global issue, therefore low-cost, highly efficient catalysts are urgently demanded for wastewater purification. We present an ultrasonic-engineered catalytic technology, which can achieve an extremely high efficiency in azo dye degradation via a tiny dosage of 0.1 g L^{-1} (only one-fifth of the normally used dosage) $Fe_{81}Si_9B_{10}$ amorphous powders (APs) with a low activation energy of 45.32 kJ mol^{-1} and a high reaction rate of 0.70291 min^{-1}. The non-destructive ultrasonic vibration (UV) treatment with very short processing times (0.43-1.08 s) amplifies degradation efficiency by an astonishing 55-fold compared to untreated APs. Combined with high-energy X-ray diffraction and small-angle neutron scattering analyses, we reveal that the UV-induced structural reconstruction at both short- and medium-range order effectively lower reaction energy barriers while accelerating charge transfer kinetics. The high-energy ultrasonic attacks promote the exposure of massive fresh active sites, which enhance the Fe^{2+}/Fe^{3+} redox circulation and thereby lead to the fast Fenton-like oxidation processes. By integrating ultrasonic physics with amorphous materials, this work develops an energy-efficient catalytic activation method, enabling sustainable water purification and innovative pollutant treatment strategies.

amorphous alloys, ultrasonic vibration, structural order, dye degradation, electronic and atomic configurations

†Equally contributed to this work
*Corresponding authors (Chenchen Yuan, email: yuancc@seu.edu.cn; Yubing Ke, email: keyb@ihep.ac.cn; Jiang Ma, email: majiang@szu.edu.cn)

Citation: J. Ruan, W. Li, C. Yuan, L. Li, W. Feng, W. He, T. Lu, F. Lan, Q. Zeng, Y. Lu, Z. Wang, X. Wu, Y. Ke, H. Yang, J. Ma, Y. Pan, and W. Wang, A highly efficient amorphous catalyst achieved by ultrasonic vibration, Sci. China-Phys. Mech. Astron. **69**, 236111 (2026), https://doi.org/10.1007/s11433-025-2845-y

1 Introduction

The widespread usage of dyes in industrial fields such as spinning, tanning, and papermaking industries has caused severe pollution to the water environment [1-5]. For water-dependent organisms like humans, organic contaminants pose serious health hazards due to their high biological toxicity and potential hazards [6,7], including carcinogenicity [8], mutagenicity [9], and bactericidal activity [10]. Accordingly, the dye wastewater has become a major environmental safety issue that needs to be addressed urgently.

In response to this issue, sewage treatment plants have set up primary, secondary, and tertiary treatment stages based on various physical, chemical, and biological reactions. However, all conventional treatment methods expose their drawbacks. The physicochemical degradation methods, such as adsorption, ion exchange, etc., still retain dye toxicity and require subsequent treatments [11,12]. Besides, it is difficult for microorganisms to completely degrade dye wastewater during the biodegradation process, which even brings a counterproductive effect that originates from their inherent toxicity, selectivity, and systemic instability [13,14]. In contrast, advanced oxidation processes (AOPs) are the most popular wastewater treatment methods currently because of their environmental friendliness and high efficiency [12]. During the Fenton-like process, powerful oxidizing agents (e.g., ·OH, $SO_4^{-}\cdot$ or $O_2^{-}\cdot$) with a high chemical reactivity and low selectivity are generated to degrade most of the organic pollutants in the wastewater, involving zero-valent metals reacting with hydrogen peroxide (H_2O_2), which ultimately achieves water purification [15-20].

During the past decade, many Fe-based crystalline catalysts like zero-valent iron Fe^0 (ZVI), zeolites, and metal-organic framework (MOF) and its derived materials have exhibited high catalytic efficiencies for the degradation of organic pollutants based on AOPs [21-23]. Recent researches reveal that Fe-based amorphous alloys, as novel ZVI materials, demonstrate a superior catalytic performance attributed to their uniquely amorphous structure. This metastable configuration favors high-density active sites and enhanced electron transfer kinetics [24,25]; meanwhile, the inherent corrosion resistance ensures sustained reactivity in dye degradation processes, which makes them outperform both crystalline alloys and conventional ZVI systems [26,27].

Fe-based amorphous alloys, as a typical disordered compound formed through the rapid melt quenching technique, trace their origins to the Fe-P-C system in 1967 [28]. A milestone was achieved in 1995 when the Fe-Al-Ga-P-C-B system overcame the barrier of the millimeter-scale bulk fabrication [29]. These materials integrate exceptional soft magnetic properties (coercivity < 1 A m^{-1}, saturation magnetization 1.5-1.7 T) [30,31], ultrahigh mechanical strength (3-4.9 GPa) [32,33], and outstanding corrosion resistance (corrosion current density as low as 10^{-7} A cm^{-2}) [34]. Their high electrical resistivity suppresses high-frequency eddy current losses, driving applications in transformers and marine corrosion-resistant components, which make them serve as promising materials for energy-efficient and low-carbon technologies in new energy infrastructure.

Among these Fe-based amorphous alloys, Fe-Si-B systems emerge as promising catalysts in Fenton-like-based AOPs [35-37]. For instance, $Fe_{73}Si_7B_{17}Nb_3$ demonstrates an outstanding efficiency for the dye degradation, achieving a rate approximately 200 times faster than that of conventional iron powders [26]. Compared with commercial catalysts, $(Fe_{0.99}Mo_{0.01})_{78}Si_9B_{13}$ [38], $Fe_{78}(Si,B)_{22}$ [25], $Fe_{78}Si_8B_{14}$ [39], and $Fe_{78}Si_9B_{13}$ [40] exhibit a better degradation performance on the azo dye solution. For instance, the removal rate of chemical oxygen demand in $Fe_{78}Si_9B_{13}$ during the degradation of wastewater with organic matter and toxic substances is 40% higher than traditional FeO materials [41].

Despite these advantages, the aging or structural relaxation during the long-term storage and service process of Fe-based amorphous alloys significantly cuts down the number of the existing active sites on the reaction interface, and causes a thick oxide layer to form on the surface. It results in a dramatic reduction of Fe^0 and reactive Fe^{2+} contents [42] and thereby a low degradation efficiency. Numerous studies show that post-process methods, e.g., annealing [43-45], dealloying [46,47], electrochemical etching [48], pulsed laser micromachining [49], etc., can accelerate the reactivity of the dye degradation process through complex physicochemical processes. Unlike traditional processes, the newly developed ultrasonic vibration (UV) method can inject energy into amorphous materials to stimulate a high potential energy state with a very short processing time of less than 1 s, which fast realizes the non-destructive modifications such as welding, manufacturing of bulk alloys from small amorphous pieces [50-53], particularly, ultrasonic-assisted catalyzing with the improved activity [54,55]. For instance, Wu et al. [54] found that the UV-treated $Fe_{78}Si_9B_{13}$ amorphous alloy demonstrates excellent electrocatalytic performance (overpotential is only 173 mV at 10 mA cm^{-2}) and great cycling stability compared with that of the sample

without UV treatment.

Therefore, the UV is adopted to treat the commercial $Fe_{81}Si_9B_{10}$ amorphous powders (APs) [56] with a thick exposed oxidized surface to simulate abandoned industrial wastes in this work. The effect of the UV treatment on the dye degradation behaviors of $Fe_{81}Si_9B_{10}$ APs was systematically investigated with various energies and times. Inspiringly, a significant improvement of the degradation efficiency of 55 times was achieved by using the $Fe_{81}Si_9B_{10}$ APs of only one-fifth of the normally used dosage after UV with an extremely short processing time of only 0.81 s. A comprehensive degradation mechanism was proposed based on the atomic and electronic structure analysis of UV-treated APs from the perspective of an ultrasonic-accelerated order and electronic structural manipulation. The underlying UV-assistant catalytic mechanism is well drawn, which proves that UV treatment is a promising preparation and post-processing method for highly efficient catalysts.

2 Methods

2.1 Preparation of UV-treated $Fe_{81}Si_9B_{10}$ powders

The original $Fe_{81}Si_9B_{10}$ APs with an average diameter of 0-10 μm were purchased, which were fabricated by the gas atomization method. The powders were subjected to post-treatment using ultrasonic vibration (UV, BRANSON 2000X), with different applied energies of 0, 250, 500, and 750 J, which correspond to the processing times of 0, 0.43, 0.81, and 1.08 s, respectively. The ultrasonic triggering force was determined to be 300 N, an amplitude of 100%, and the working pressure of 400 kPa. For convenient comparison, the samples with various energy states were denoted as 0, 250, 500, and 750 J, respectively.

2.2 Dye degradation measurements

Commercially, methylene blue (MB, $C_{16}H_{18}C_1N_3S{\cdot}3H_2O$) and Rhodamine B (RhB, $C_{28}H_{31}C_lN_2O_3$) were purchased from Keqi Chemical Technology Co., LTD. The AO7 ($C_{16}H_{11}N_2NaO_4S$) was purchased from Jiangsu Aikang Biomedical Research and Development Co., Ltd. H_2O_2 (30%), sulfuric acid (H_2SO_4, 95%-98%), sodium hydroxide (NaOH), and *t*-butyl alcohol (TBA, >99.0%) were employed as analytical reagent grades in this experiment.

During the degradation experiment, the 250 mL MB dye solution with a concentration of 100 mg L^{-1} was prepared in a 500 mL beaker, and simultaneously added H_2O_2 to adjust the concentration to 5 mM. The adjustment of the pH value of the solution was achieved by using 0.1 mol L^{-1} H_2SO_4 and 0.1 mol L^{-1} NaOH. Then, the dye solution was placed in a thermostatic water bath with a heat controller. The temperature of the solution in the beaker was maintained stable at room temperature 25°C. Finally, the APs were added to the solution at a concentration of 0.1 g L^{-1}, for ensuring the effective degradation process, a stirrer with a fixed speed of 450 r min^{-1} was used to avoid the aggregation of powders. During each time interval, 3 mL of the degraded dye solution was withdrawn by using a syringe, filtered through a filter membrane with a diameter of 0.22 μm, and then injected into a transparent cuvette to test their absorbance spectra (200-800 nm) through utilizing an ultraviolet visible spectrophotometer (Shimadzu UV-1280). Notably, the optimal experimental parameters, including the pH of the solution, H_2O_2 concentration, and reaction temperature, were determined by a series of experiments. Additionally, a range of individual and mixed dyes was degraded to verify the catalyst's high efficiency and broad applicability. In order to further detect the main reactive oxidative species, radical quencher experiments were conducted using TBA (·OH scavenger) [57].

2.3 Surface morphology and structural characterization

The obtained samples were examined by various analytical techniques. X-ray diffraction (XRD, Brucker, D8-DISCOVER) with Cu Kα radiation (λ = 0.15405 nm) was used to identify the amorphous nature. The surface morphology and elemental distribution of the powders before and after degradation were observed by scanning electron microscope (SEM, Hitachi Regulus 8100) equipped with the energy dispersive X-ray spectrometer (EDS). Due to the usage of silicon wafers as sample support substrates in the SEM testing and the difficulty of quantitative analysis of light elements like B by EDS, the content of both Si and B is not included. The microstructural measurements were performed by using a high-resolution transmission electron microscope (HRTEM, FEI Tecnai G2 F30) with an accelerating voltage of 300 kV. To quantitatively characterize the localized ordering of the samples, we have randomly selected a region with the area of 20 × 20 nm^2 in the HRTEM image, and then divided it into 100 boxes with a single size of 2 nm × 2 nm, which closes to the smallest size of the observed crystal-like order. Subsequently, the short-range order of each cell was demonstrated by employing two-dimensional autocorrelation functions (2D ACFs).

2.4 High-energy XRD measurements

High-energy XRD experiments with a maximum wave vector momentum transfer of q = 9 $Å^{-1}$ were conducted for detecting more structural signatures. The 2D images were integrated with the software of Fit2D and Dioptas, and the structure factor $S(q)$ and reduced pair distribution $G(r)$ were obtained via the program package PDFgetX3.

2.5 Small-angle neutron scattering measurement

Small-angle neutron scattering (SANS) measurements were performed on the Small-angle Neutron Diffractometer at China Spallation Neutron Source (CSNS) to deeply detect the microscopic structure in the range of 1-100 nm of the sample, originating from the heterogeneity of density and composition. The incident neutrons with a wavelength of 3-8.6 Å were defined by a double-disc bandwidth chopper, which is collimated to the sample by a pair of apertures. The experiment used the sample to detector distance of 5 m and a sample aperture of 8 mm in diameter. The two-dimensional ^{3}He tubes array detector allows covering a wide Q range from 0.004 to 1.2 Å^{-1}. We collected approximately 50 min scattering information for each sample, including the empty sample holder [58] and sample cell. The scattering data were set to absolute units after normalization, transmission correction, and standard sample calibration.

The resulting 1D scattering profiles were fitted to a structural model to assess the evolution of nanoprecipitates within the samples. This model incorporates a log-normal size distribution of spherical particles, with adjustments made for a flat background to accurately represent the scattering data. The SANS intensity is formulated as:

$$I(Q) = \left(A / \langle V \rangle\right) \times \int_0^\infty f(R)(\Delta\rho)^2 V^2 (F(Q,R))^2 \mathrm{d}R + B, \quad (1)$$

where A is the scale factor accounting for the number density of precipitates, $<V>$ is the average volume of precipitates, $\Delta\rho$ is the difference in scattering length density between the precipitates and the matrix, B is the background, and $F(Q, R)$ is the spherical form factor of the precipitated phase. $f(R)$ refers to the log-normal size distribution function for precipitates, which can be described as:

$$f(R) = (1 / \sigma R\sqrt{2\pi}) \times \exp\left[-\left(\ln R - \ln R_{\mathrm{med}}\right)^2 / 2\sigma^2\right], \quad (2)$$

where R_{med} and σ refer to the median radius and polydispersity of the precipitates, respectively. Moreover, the mean precipitate radius (R_{avg}) is given by the equation [59,60]: $R_{\mathrm{avg}} = R_{\mathrm{med}} \times \exp\left(\frac{\sigma^2}{2}\right)$.

2.6 Relaxation enthalpy measured by DSC

The thermal properties and phase transition behavior of APs were analyzed by differential scanning calorimeter (DSC, Netzsch 404 F3) from 300 to 1500 K with a heating rate of 20 K min^{-1} under an argon atmosphere. Additionally, the specific steps for measuring the relaxation enthalpy (ΔH_{rel}, heat release before the glass transition) using DSC are as follows: The test involves two heating cycles. Firstly, the samples are heated above crystallization temperature (T_{x}) and then cooled to ambient temperature to fully release the relaxation heat. Subsequently, the second heating is conducted under the same parameters. The ΔH_{rel} is derived by subtracting the heat absorption/release curve of the second cycle from that of the first.

2.7 XPS depth analysis

X-ray photoelectron spectroscopy (XPS, Thermo Scientific ESCALAB 250Xi) was used to measure and analyze the electronic structure and chemical states of powder surface elements before and after degradation experiments. XPS depth profiling examined the vertical distribution of elemental chemical information within APs. It involved etching and thinning the sample to a certain depth using an argon ion gun (with a 500-micrometer spot size, 500 eV ion energy, and an etching rate of 0.2 nm s^{-1}), followed by spectral analysis.

2.8 FTIR analysis

The degradation reaction products of $Fe_{81}Si_9B_{10}$ APs were identified by Fourier transform infrared (FTIR, Thermo Scientific Nicolet iS10) in the wavelength range of 400-4000 cm^{-1}, and the empty chamber was adopted as a baseline before performing the FTIR measurement.

2.9 Electrochemical measurements

Electrochemical studies were conducted using the CHI660E Electrochemical Work Station, with a three-electrode system consisting of a platinum plate as the counter electrode, a saturated calomel electrode as the reference electrode, and samples as the working electrode. After the open circuit potential (OCP) stabilizing, the sample powders were attached to carbon paper with a working area of 1 cm^2 for electrochemical impedance spectroscopy (EIS) testing in the frequency range of 1000 kHz to 0.01 Hz, and polarization corrosion experiments were conducted in the potential range of −0.7 to 1.5 V. The entire test was conducted in MB solutions with a pH of 3 and a concentration of 100 mg L^{-1}.

3 Results and discussion

3.1 Degradation behaviors of $Fe_{81}Si_9B_{10}$ APs under UV treatments

Figure 1 shows dye degradation behaviors of $Fe_{81}Si_9B_{10}$ APs under the UV treatment (a schematic of UV devices and dye wastewater purification processes is included in Figure S1). Herein, the transducer of UV equipment converts high-frequency electrical energy (at a frequency of 20 kHz) into a stable ultrasonic signal. Subsequently, the booster amplifies the amplitude of the ultrasonic vibrations. Finally, the sonotrode concentrates and delivers the vibrational energy into

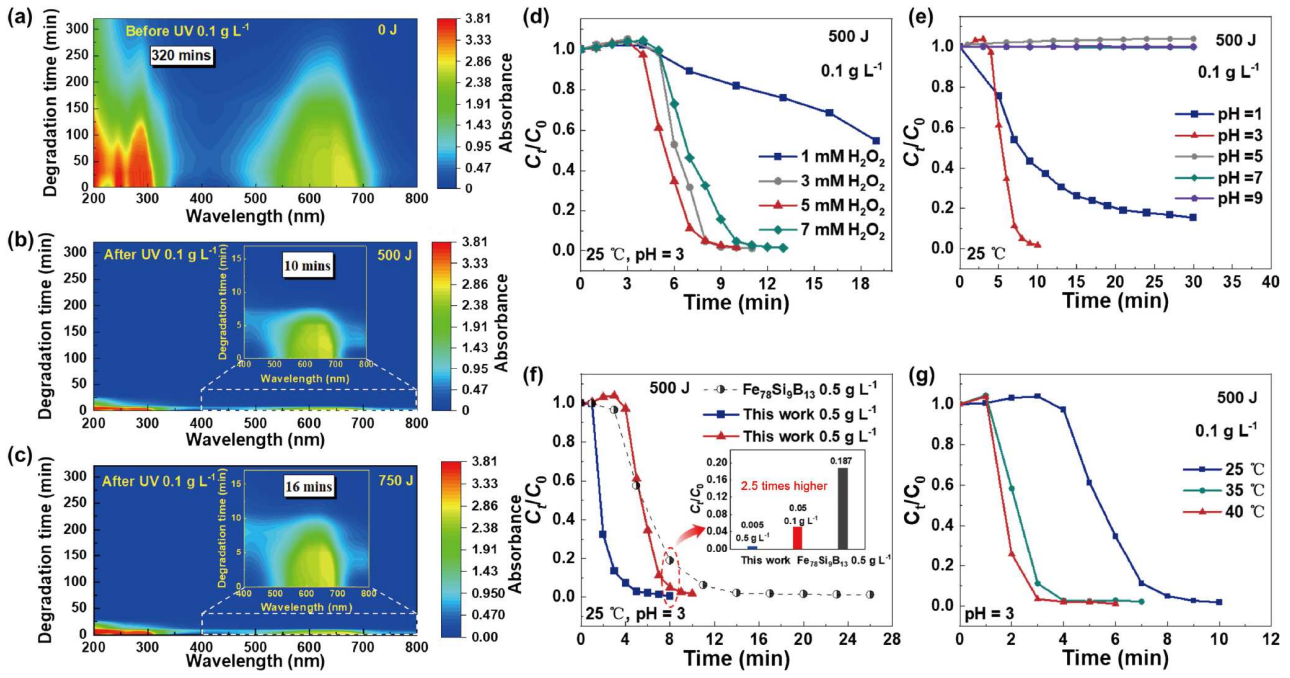

Figure 1 (Color online) Ultraviolet-visible absorption spectra of degradation MB solution during reaction for 0 (a), 500 (b), and 750 J (c) APs. The insets of (b) and (c) correspond to enlarged ultraviolet-visible spectra in the range of 400-800 nm for 500 and 750 J APs, respectively. The effect of H_2O_2 concentration (d), pH (e), catalyst dosage (f), temperature (g) on degradation (previously reported 500 J $Fe_{78}Si_9B_{13}$ with a dosage of 0.5 g L^{-1} for comparison in (f). Reproduced with permission from ref. [55]. Copyright©2020, Elsevier). The inset in (f) refers to the C_t/C_0 of 500 J APs with dosages of 0.1 and 0.5 g L^{-1}, as well as the previously reported $Fe_{78}Si_9B_{13}$ with a dosage of 0.5 g L^{-1} at 8th min during the degradation process.

the sample within a pre-set time. Notably, the output of vibrational energy can be flexibly adjusted through the processing time. In this work, the processing time is adjusted to 0.43, 0.81, and 1.08 s, corresponding to applied energies of 250, 500, and 750 J, respectively. The as-cast and UV-treated $Fe_{81}Si_9B_{10}$ samples are thereby denoted as 0, 250, 500, and 750 J APs as below. The amorphous nature of powders before and after UV is checked by XRD using Cu Kα (λ = 0.15405 nm) (Figure S2). Afterwards, these APs are adopted to degrade azo dye solutions, taking MB with high antioxidant resistance [61] for example.

Figure 1(a)-(c) give the ultraviolet-visible absorption spectra during MB degradation by using as-cast (0 J) and UV-treated (500 and 750 J, other data including 250 J are summarized in Figure S3) $Fe_{81}Si_9B_{10}$ APs as catalysts under the environment temperature of 25°C and pH of 3. Notably, the samples demonstrate much higher degradation efficiency after UV treatments, especially for 500 J APs, wherein the characteristic absorption peaks at 664, 292, and 245 nm completely disappear just within 10 min, see the inset in Figure 1(b). The occurrence of Fenton-like reaction during the MB degradation process is verified by TBA (·OH scavenger) (Figure S4).

Take 500 J APs as an example, the MB degradation under different H_2O_2 concentrations, pH, sample dosages, and temperatures are demonstrated in Figure 1(d)-(g) via C_t/C_0 versus time curves, where C_0 and C_t refer to the solution concentration of MB at the reaction time 0 and t, respectively. Based on the experimental measurements, the optimal degradation conditions like H_2O_2 concentration, pH, and reaction temperature are determined to be 5 mM, 3, and 25°C, respectively (A more detailed explanation of the optimal degradation conditions is provided in Figure S5). More interestingly, we find that the degradation efficiency of 500 J $Fe_{81}Si_9B_{10}$ APs with a dosage of 0.5 g L^{-1} is about 2.5 times higher than our previously reported value of $Fe_{78}Si_9B_{13}$ APs at the same applied UV energy [55], see Figure 1(f) and the corresponding inset. Therefore, a lower dosage of 0.1 g L^{-1} with a longer degradation time is selected to make the data collection more convenient.

Figure 2 displays the degradation behaviors of APs under different UV processing energies. No obvious change in MB concentration was observed in 0 J APs within 60 min. As shown in Figure 1(a), the whole degradation process of MB consumes almost 320 min for APs at the as-cast state. In contrast, the UV treatment evidently reduces the decolorization consuming time of APs catalysts up to about 32 times. The degradation consuming time is obviously shortened from 320 min of as-cast APs to 35 min of 250 J APs and only 10 min of 500 J APs, then increases slightly again to 16 min of 750 J APs with longer UV processing time, see Figure 2(a). Under the same reaction conditions, various

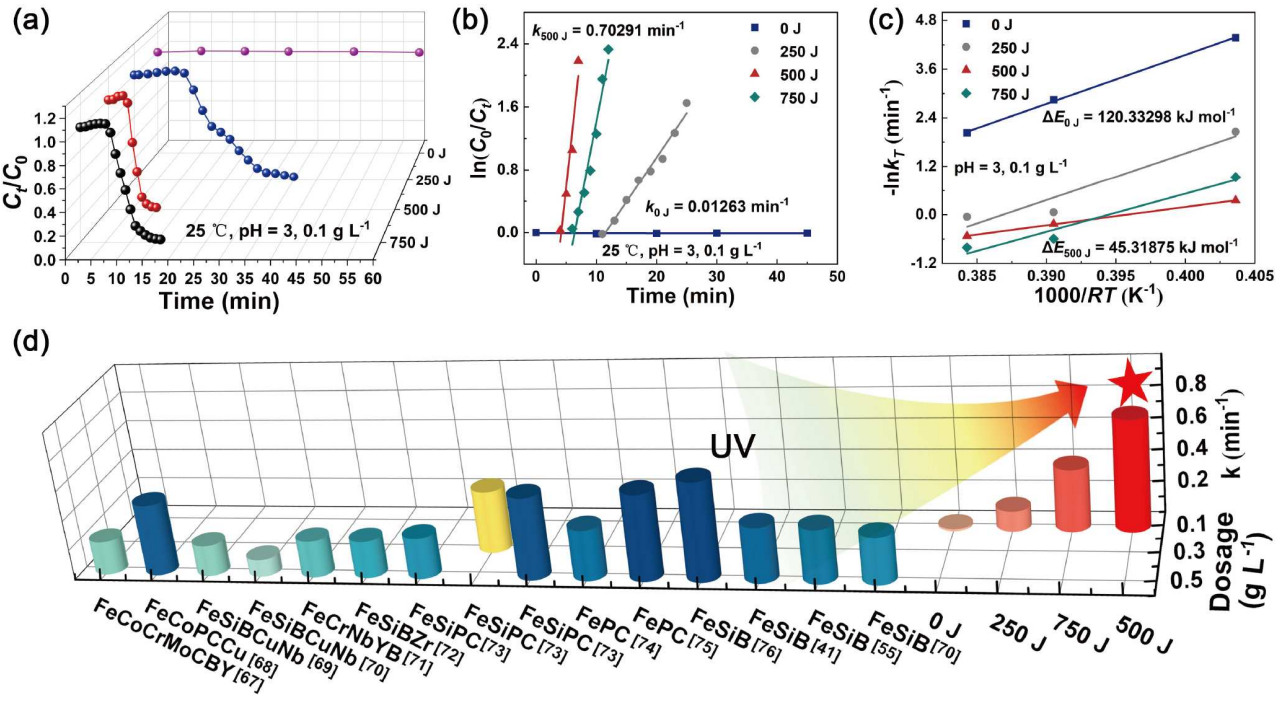

Figure 2 (Color online) The effect of UV energies on degradation. (a) C_0/C_t and (b) $\ln(C_0/C_t)$ versus t and (c) $-\ln k_T$ versus $1000/RT$ for $Fe_{81}Si_9B_{10}$ APs with applied UV energies ranged from 0 to 750 J. (d) Summarization of k in present work and other reports [41,55,67-76] (see all data in Table S3).

other azo dyes, including RhB, acid orange 7, as well as their mixtures, also achieve rapid degradation with a degradation efficiency exceeding 95% within 18 min by using the 500 J APs as catalysts (Figure S6). In addition, the degradation efficiency remains high (over 97%) even after repeated uses (Figure S7).

The degradation reaction constant (k_{obs}) is used to evaluate the degradation capability more quantitatively, see Figure 2(b), derived by the linear fitting of $\ln(C_0/C_t)$ versus t based on the pseudo-first-order equation (eq. (3)) [20]:

$$\ln\frac{C_0}{C_t} = k_{obs}t. \tag{3}$$

As shown in Figure 2(b) and Table S1, the k_{obs} values of 0, 250, 500, and 750 J APs are determined to be 0.01263, 0.12752, 0.70291, and 0.39322 min^{-1}, respectively. Notably, the 500 J APs demonstrate a significantly enhanced degradation efficiency around 55 times higher than that of the as-cast one. Due to the thermal activation behavior of AOPs, the increase of temperature during degradation accelerates the motion of particles, which boosts the probability of contact between reactants, and accordingly results in higher decolorization efficiency [62], see Figure S8 and Table S1. Therefore, the thermal activation energy (E_a) is another important indicator to evaluate the catalytic reaction, which can be calculated from the Arrhenius equation (eq. (4)) as follows [63]:

$$\ln k_{obs} = -\frac{E_a}{RT} + \ln A, \tag{4}$$

where R is the ideal gas constant, T is the reaction temperature, and A is the pre-exponential factor. Figure 2(c) illustrates the linear fitting of $-\ln k_T$ versus $1000/RT$ as well as the derived E_a. Generally, the activation energy E_a is around 60-250 kJ mol^{-1} for Fenton-like reaction during the degradation of azo dyes with AOPs [64]. A low E_a facilitates atoms overcoming their intrinsic energy barriers, thus, more active sites in catalysts can be stimulated more easily during degradation. As demonstrated in Figure 2(c) and Table S2, 500 J APs exhibit a minimum value of E_a (45.32 kJ mol^{-1}) among all studied APs samples, which is just one third of that of as-cast APs. More importantly, the E_a of 500 J APs is remarkably lower than those of other reported Fe-based amorphous catalysts as well, e.g., $Fe_{78}Si_9B_{13}$ (56.95 kJ mol^{-1}) [65], $Fe_{73}Si_7B_{17}Nb_3$ (78 kJ mol^{-1}) [26], and $Fe_{50}Ni_{30}P_{13}C_7$ (46.6 kJ mol^{-1}) [66]. Evidently, 500 J APs with the highest k_{obs} and the lowest E_a, emerge as the optimal catalyst for the dye degradation in this work. More importantly, compared with other previously reported Fe-based amorphous catalysts for azo dye degradation [41,55,67-76], our as-prepared UV APs only require an extremely low dosage of 0.1 g L^{-1} (only one-fifth of the normally used dosage) to achieve a fast degradation rate, see Figure 2(d) and Table S3. It is observed that the k_{obs} of the 750 J $Fe_{81}Si_9B_{10}$ APs are approximately 2-fold higher than that of the previously reported FeSiB-based amorphous catalysts. Therefore, 500 J APs can be considered as one of the highest effective catalyst candidates for azo dye degradation till now.

3.2 Evolution of surface morphologies during degradation

The dye degradation by using Fe-based amorphous catalysts is regarded as a surface-mediated process [77]. Hence, the surface morphology of UV APs before and after degradation is recorded by scanning electron microscopy (SEM), see Figures 3 and 4. It is found that as-cast (0 J) APs mainly exhibit a smooth spherical shape (Figure 3(a)-(c)), while after UV (500 J), joint particles are more likely to be constructed with more irregular shapes such as ellipsoidal and dumbbell morphologies due to the UV-assistant welding process [78]. Based on the statistics of particle size distributions, the average particle size of 0 J APs is determined to be (1.66 ±1.15) μm (Figure 3(d)). In contrast, the average particle size of 500 J APs increases to (2.63 ±2.03) μm, along with white dots-like protrusions densely distributed on the particle surface as well as a small number of peelings [79], see Figure 4(a)-(d), in consistent with the particle shape analysis above.

Figures 3(e) and 4(e) show elemental distributions detected by the energy dispersive spectrometer (EDS) of SEM, and the statistical analysis of element content is listed in Table S4. Due to the usage of silicon wafers as sample support substrates in the SEM testing and the difficulty of quantitative analysis of light elements like B by EDS, the content of both Si and B is not included. It can be seen that all constituent elements exhibit a uniform distribution. The relatively high oxygen content in all APs samples indicates that an oxide layer is formed on the particle surface. It is mainly ascribed to the fact that the APs samples are prepared by the aerosol method with long-term storage, which can be used to simulate Fe-based amorphous industrial wastes after long-term service. This thick oxide layer, therefore, suppresses the Fenton-like reaction by covering active sites, resulting in a poor degradation activity of 0 J APs [73]. Nevertheless,

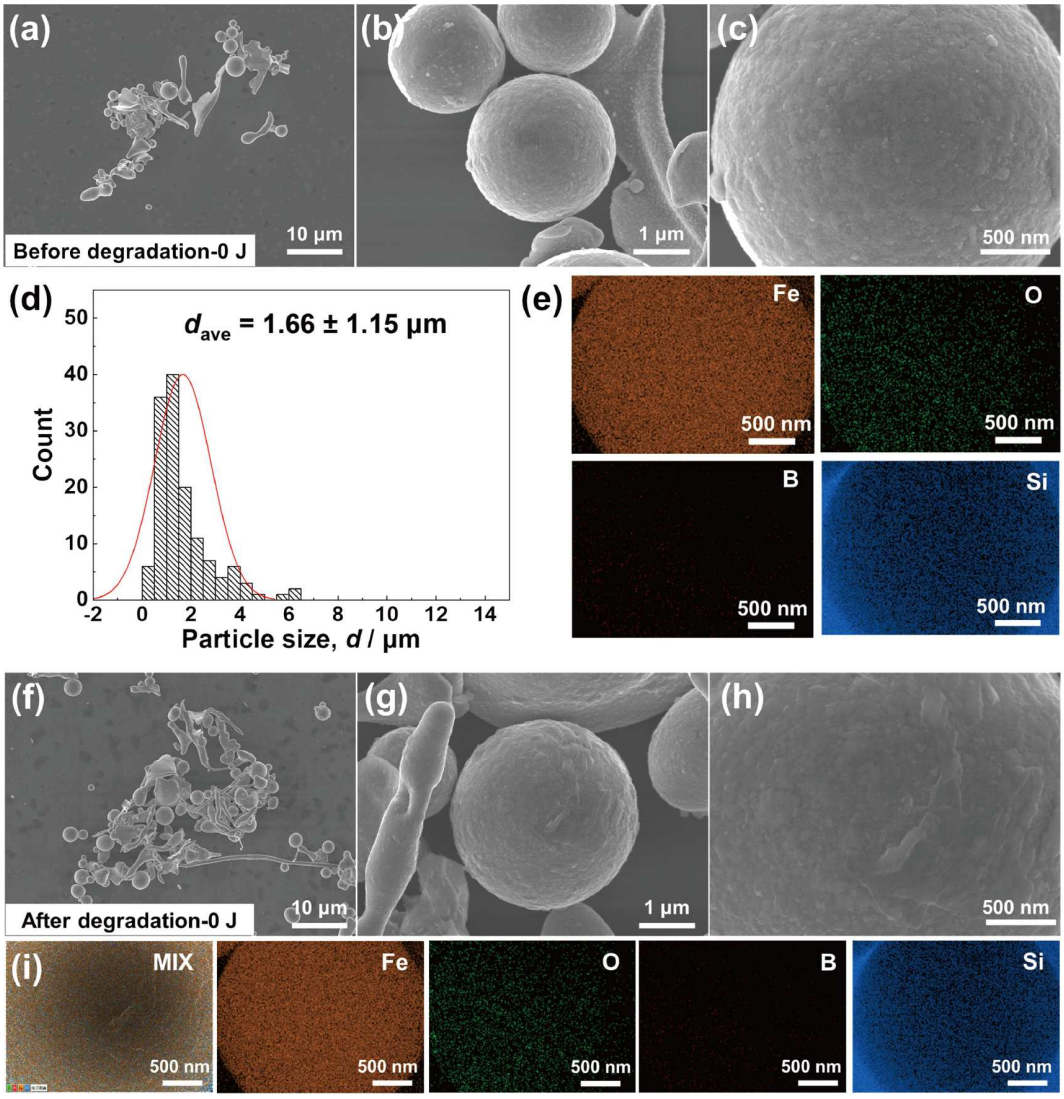

Figure 3 (Color online) Surface morphologies, particle size distribution, and elemental distributions of 0 J APs before (a)-(e) and after degradation (f)-(i).

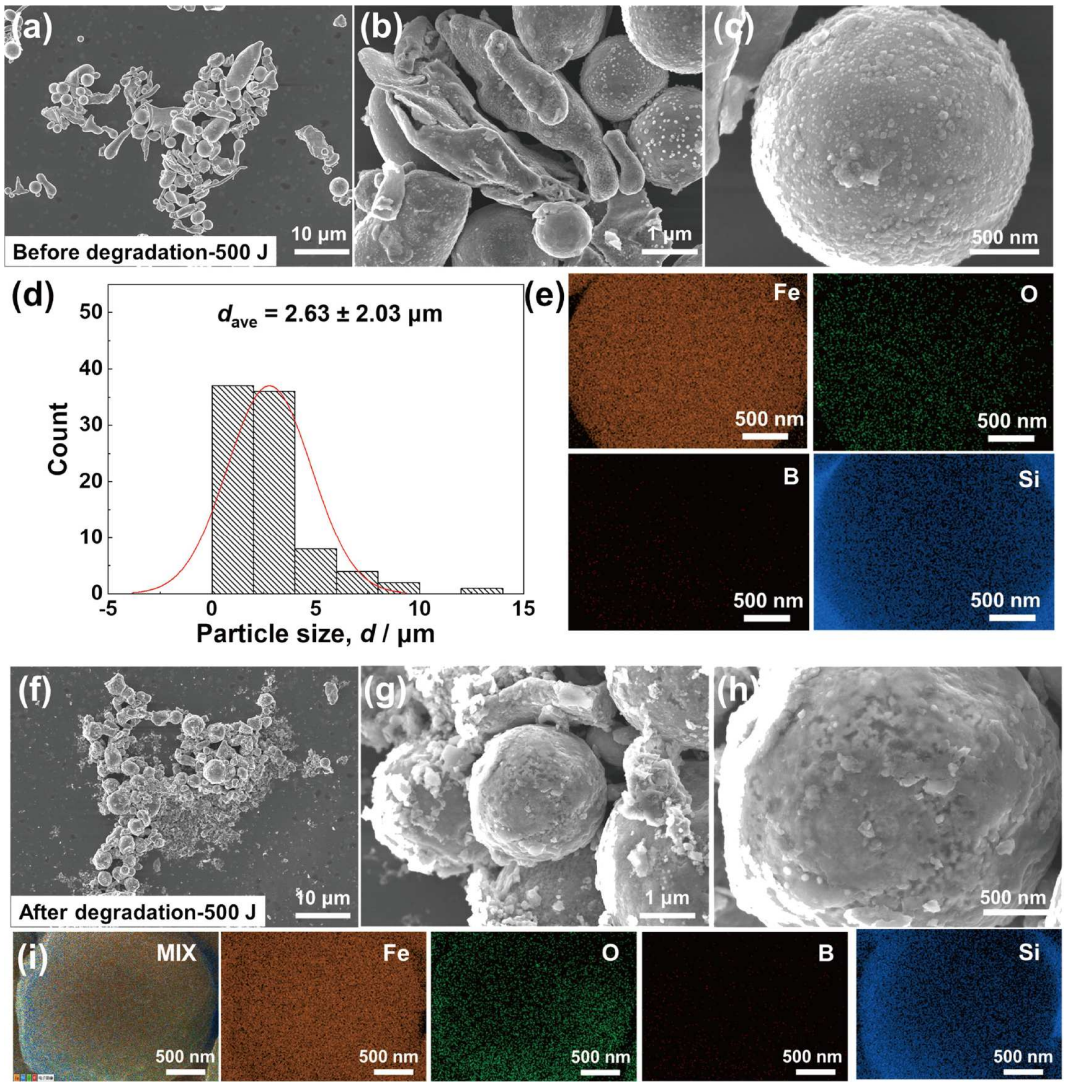

Figure 4 (Color online) Surface morphologies, particle size distribution, and elemental distributions of 500 J APs before (a)-(e) and after degradation (f)-(i).

500 J APs undergo highly effective AOPs, wherein the oxide layers are destroyed during UV treatments and give rise to multiple protrusions and cracks on the particle surface. The UV processing leads to the exposure of more active sites, which effectively restores catalytic activity.

Figures 3(f)-(h) and 4(f)-(h) display SEM images of 0 and 500 J APs after degradation, respectively. It is found that the surface morphology of 0 J APs does not change significantly except for some peelings that appeared on the particle surface, see Figure 3(h), whereas more features, evidenced by flocculent-like fragmented morphologies, display on the surface of 500 J APs after reaction, along with the vanished white protrusions. Moreover, the spherical particles' surface of 500 J APs reveals extensive corrosion with unevenly sized pores distributed on fragmental oxide layers, see Figure 4(f)-(h). Comparing with the 0 J sample (Figure 3(i)), the intensified oxidation reaction of 500 J APs results in a reduction of Fe contents with increasing O contents, as shown in Figure 4(i) and Table S4.

3.3 Structural reconstruction stimulated by UV

The microstructure of APs under UV is detected by the high-energy XRD, see the normalized $S(q)$ curves in Figure 5(a). All samples exhibit broad amorphous humps within the range of 2-4 $Å^{-1}$, except for the 750 J APs with sharp crystalline peaks at 6.24, 6.98, and 8.26 $Å^{-1}$, indicating its more ordered state. It is observed that the first peak position of $S(q)$ slightly shifts from 3.09 to 3.11 $Å^{-1}$ of the 750 J APs, which is mainly ascribed to the packing densification effect during the UV processing [80]. To investigate the structural information of APs in real space, the reduced pair distribution function ($G(r)$) is derived by Fourier transformation of $S(q)$, see Figure S9. It is clear that different from the crystallized 750 J APs, the $G(r)$ curves of 0, 250, and 500 J APs are very close to the structural signature of metallic melts, suggesting

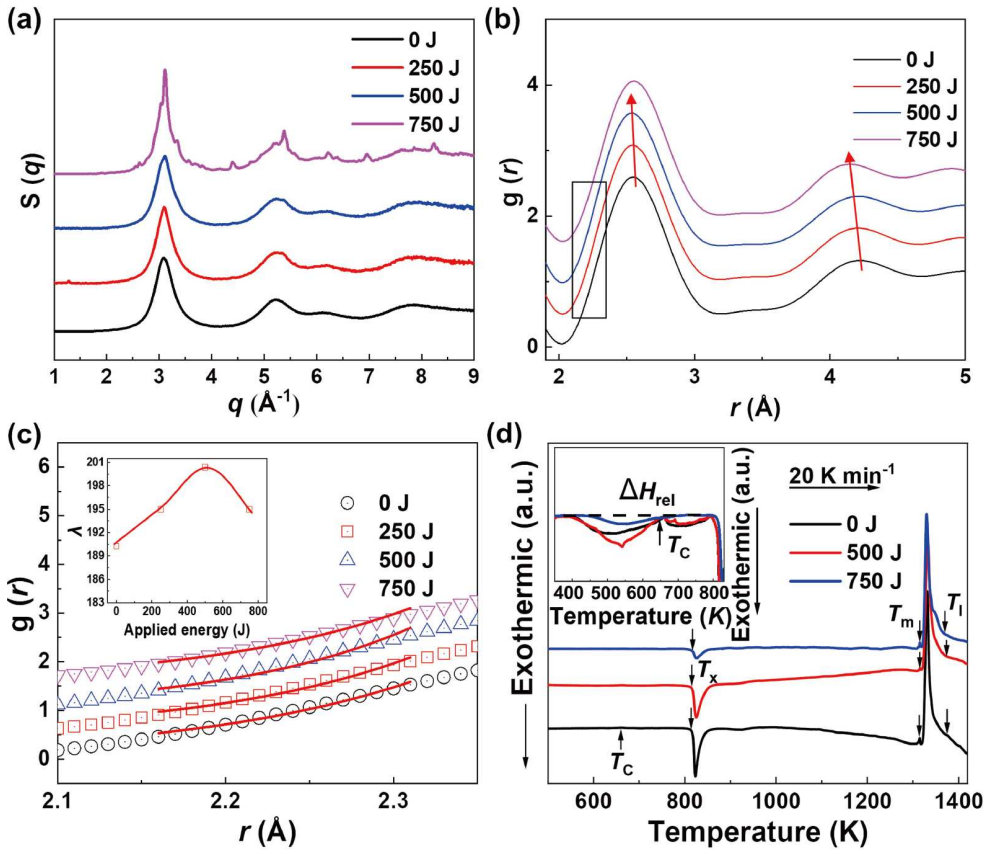

Figure 5 (Color online) $S(q)$ (a) and $g(r)$ (b) curves for all samples. (c) The enlarged image of the selected area in (b) (marked by a black square). The inset shows the variation of λ with ultrasonic energy. (d) DSC curves of 0, 500, and 750 J APs. The inset shows enthalpy recovery measurements.

their high degree of disorder [80]. Based on $G(r)$, the pair correlation function ($g(r)$) can be calculated by using the following equation [81]:

$$g(r) = \frac{G(r)}{4\pi\rho_0 r} + 1, \tag{5}$$

where ρ_0 is the mean atomic number density of the sample, which can be approximately expressed by the weighted average density of each atom. In consistent with $S(q)$, the shift of the main peak and the second peak representing the first and second coordinate shells to a low position can be found for the UV-treated APs (except for the first peak of the crystallized 750 J APs), see Figure 5(b). According to the radial distribution function [82]: $V(r)/k_BT = -\lg(r) \sim -\ln(r-\sigma)^{\lambda}$ the potential of mean force between two atoms can be well described. In this function, k_B is the Boltzmann constant, σ refers to the mutual separation between two ions, and the interaction energy is practically infinite. If the separation of ions is very close, $V(r)$ reduces to the short-range-order (SRO) part of the ion-ion repulsion. Therefore, the λ is proportional to the steepness of the effective repulsion. Figure 5(c) gives the corresponding linear fitting of the left flank of $g(r)$ curves. As shown in the inset of Figure 5(c), the λ gradually increases from 190.27 to 200.39 as the UV time ascends from 0 to 0.81 s of the 500 J APs, indicating its steepest repulsion. With further UV treatment, the λ dramatically declines to 194.98 due to the densified ordering processing of 750 J APs.

The amorphous nature of APs is further confirmed by differential scanning calorimetry (DSC) traces (Figure 5(d)). A small flat endothermic peak appears before sharp exothermic peaks that represent crystallization, corresponding to a distinct glass transition behavior, see the inset of Figure 5(d). Herein, Curie temperature (T_C) of 660 K and crystallization temperature (T_x) of 810 K for $Fe_{81}Si_9B_{10}$ APs are marked by black arrows in Figure 5(d), and listed in Table S5, both of which are barely changed after UV. To quantitatively assess the structural change after UV, the ΔH_{rel} is estimated according to: $\Delta H_{rel} = \int(\mathrm{d}Q/\mathrm{d}t)\mathrm{d}T$, where ΔH_{rel} is the relaxation enthalpy change [83,84]. The values of ΔH_{rel} are included in Table S5, which are 1.837, 2.169, and 0.635 kJ mol^{-1} for 0, 500, and 750 J APs, respectively. It is worth noting that 500 J APs exhibit a larger relaxation enthalpy of 2.169 kJ mol^{-1} than the others. It implies that more excess free volumes ($\Delta x \propto \Delta H_{rel}$) [85] are generated in 500 J APs during UV treatments, corresponding to a much higher energy state located in the potential energy landscape (PEL)

associated with the structural rejuvenation [86,87]. This phenomenon coincides with our previous studies that the UV treatment facilitates structural rejuvenation via the redistribution of the local density [76], which reduces E_a and meanwhile enhances the activity of APs catalysts. The loosely packed configurations and positive excess free volume of the rejuvenated 500 J APs might be associated with the significant steep repulsion due to its high λ [82,88]. By further injecting high energy into APs during UV, this rejuvenated state gradually transforms to a more densely ordered state, as indicated by the reduction of both λ and ΔH_{rel}.

To further understand the deteriorative degradation performance of APs upon a higher UV energy and longer processing time, we utilize a transmission electron microscope (TEM) to further analyze the microstructural characteristics of the UV-treated samples, as illustrated in Figure 6. The inset of Figure 6(a) shows a typical halo, further verifying the amorphous nature of 0 J APs. After UV, the selected area electron diffraction (SAED) patterns of 500 J APs emerge with detectable scattered diffraction spots (Figure 6(b)). While for 750 J APs (Figure 6(c)), diffraction rings with spots corresponding to the (110), (111), and (221) planes of FeSi and α-Fe phases clearly appear (Figure 6(d)). It is suggested that the UV treatment induces an evident crystallization process. Some small seed crystals or nanocrystals grow in the glassy matrix, and their content increases with the increase of UV processing energies and time, especially for 750 J APs, see Figure 6(e). The notable lattice regions are marked by different colored squares (defined as the regions of 1, 2, 3, and 4). The lattice spaces are 0.30, 0.25, and 0.15 nm attributed to the (110), (111), and (221) planes of FeSi (Region 1, 2, 3), while a lattice spacing of 0.21 nm corresponds to the (100) plane of α-Fe nanoparticles (Region 4). Coincidently, with increasing UV processing time up to 1.08 s, the broad diffraction peak in XRD patterns that represents the amorphous nature of 750 J APs becomes slightly narrower and sharper, see Figure 5(a), implying the precipitation of a large number of nanocrystals within the amorphous matrix. The nanocrystal precipitation for 750 J APs is proposed to be attributed to the structural relaxation under UV treatments [89]. From the perspective of PEL [86], the glassy system shows low Gibbs free energy, and the internal atomic rearrangement needs to overcome a large energy barrier, which contributes to the remarkable decrease of active sites in 750 J APs. Meanwhile, it results in a reduction of the stored relaxation enthalpy about 60% (Table S5), in good agreement with the significant decrease of crystallization enthalpy (ΔH_x) [90] from 5.175 kJ mol^{-1} of 0 J APs to 1.216 kJ mol^{-1} of 750 J APs as shown in the inset DSC curves of Figure 5(d), where the exothermic peaks related to crystallization gradually go down with increasing UV processing energies.

Furthermore, two-dimensional autocorrelation function

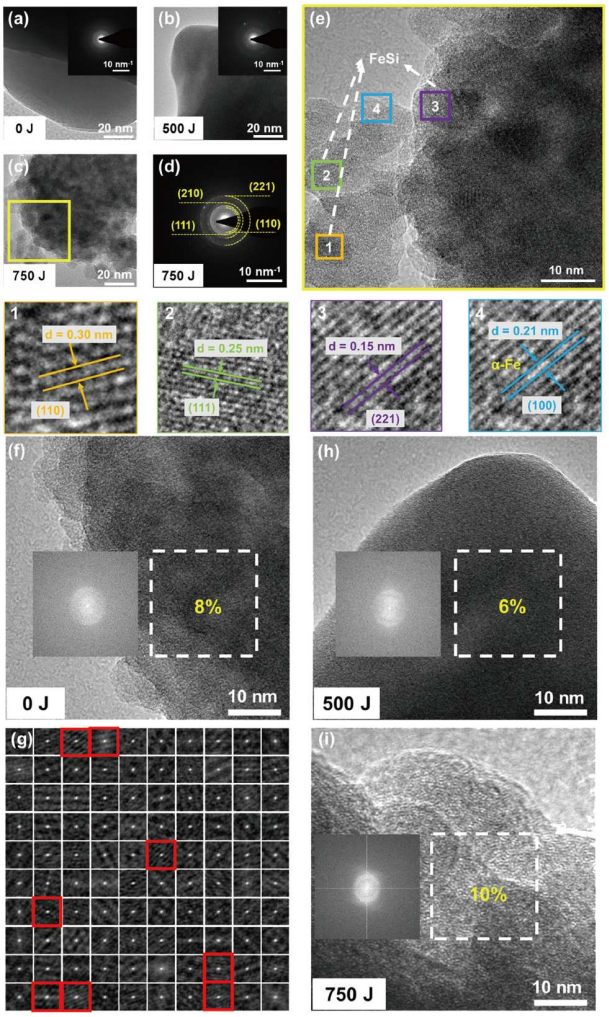

Figure 6 (Color online) HRTEM images and SAED patterns of 0 (a), 500 (b), and 750 J (c)-(e) APs, respectively. The magnified selected areas in (e) (marked by colored squares and named 1, 2, 3, and 4). HRTEM image (f) and 2D-ACFs (g) of 0 J APs, the corresponding insets show the FFT-filtered images of the selected areas. HRTEM images of 500 J (h) and 750 J (i) APs, the corresponding insets show the FFT-filtered images of the selected areas.

(2D-ACF) analyses based on a high-resolution transmission electron microscope (HRTEM) are adopted to gain an in-depth insight into these locally ordered configurations in the amorphous matrix. Figure 6(f), (h), and (i) display the HRTEM images of 0, 500, and 750 J APs. The insets show fast Fourier transform (FFT) patterns of the selected regions (marked by white dotted squares). All selected HRTEM images reveal maze-like patterns with no significant crystalline phases. Simultaneously, FFT pictures of APs samples all show a typical halo that stands for an amorphous structure. Notably, more diffraction spots are shown in the FFT pattern of 750 J APs compared to 0 and 500 J APs, indicating its higher degree of structural order. Afterwards, each selected white square is divided into 100 cells with a size of 2 nm × 2 nm, which is close to the minimum size of the

observed medium-range order [91,92]. Subsequently, each cell is directly converted to 2D-ACF to estimate its crystal-like order (Figure 6(g) and Figure S10). Statistical analysis reveals that 750 J APs show a total area fraction of ordered configuration units of about 10%, which significantly surpasses that of both 0 (8%) and 500 J (6%) APs, indicating that the 750 J sample possesses the most ordered atomic configurations among three APs samples [93].

To systematically analyze ordered structural signatures of samples, a series of small angle neutron scattering (SANS) measurements, which are the advanced technique to detect the microstructural characteristics of the materials and their distribution within the range of 1 to 100 nm, were conducted as well. Figure 7(a)-(d) shows the 2D scattering patterns collected within 50 min of 0, 250, 500, and 750 J APs, respectively. The corresponding SANS data is obtained by globally integrating the 2D scattering data, as shown in Figure 7(e). It is found that SANS profiles for the 0 and 250 J APs are almost overlapped, indicating their similar structural characteristics from perspectives of chemistry and density. Intriguingly, with further increasing UV energies and time, the SANS scattering intensity gradually decreases. Sarac et al. [94] found that the rejuvenation during thermoplastic forming is related to the structural disordering transition in amorphous alloys, which can be evidenced by a decrease in the medium-range order (MRO) in the normalized intensity variance. The UV treatment plays a similar role as the thermoplastic forming in this work, elevating the energy state of 500 J APs (Figure 5(d)), accompanied by the structural rejuvenation. Nevertheless, the 750 J APs show a slight reduction of SANS intensity over a Q range of 0.03-0.1 Å^{-1}. These abnormal nanoscale density fluctuations of the UV-induced ordered samples are analogous to the findings of Kang et al. [95], where the reduction in structural heterogeneity is attributed to the ordering behavior of converting the geometrically frustrated into more favored motifs through thermally activated relaxation. Furthermore, to investigate the evolution of the ordered particle size under UV, the size distribution of the MRO and their temporal evolution are demonstrated in Figure 7(f) and (g), where R_{avg} is the mean radius of these spherical MRO precipitates. With increasing UV energies, the maximum frequency diameter of MRO gradually increases from ~2.8 to 5.0 nm. The R_{avg} is 5.3, 6.29, 6.06, and 6.78 nm for 0, 250, 500, and 750 J, respectively. It has been reported that MRO clusters tend to be inherited from as-quenched melts due to the strong structural and dynamical heterogeneity in metalloid/non-metallic-containing systems [96-98]. As shown in Figure 7(f), these inherent MROs with small average sizes are pronounced in the as-cast APs. Upon applying UV, these inherited MRO clusters with small sizes are destroyed along with the high-energy injection, gradually evolving to more heterogeneously distributed larger MRO configurations during the UV-induced structural rejuvenation, see Figure 7(f) and (g). With the increase of UV energy from 250 to 500 J, the number of these newly generated MROs starts to grow. However, with more energies injected inside APs, further UV treatment then leads to the evolution of these configurations into more ordered crystalline configurations.

The obvious structural ordering induced by UV mentioned

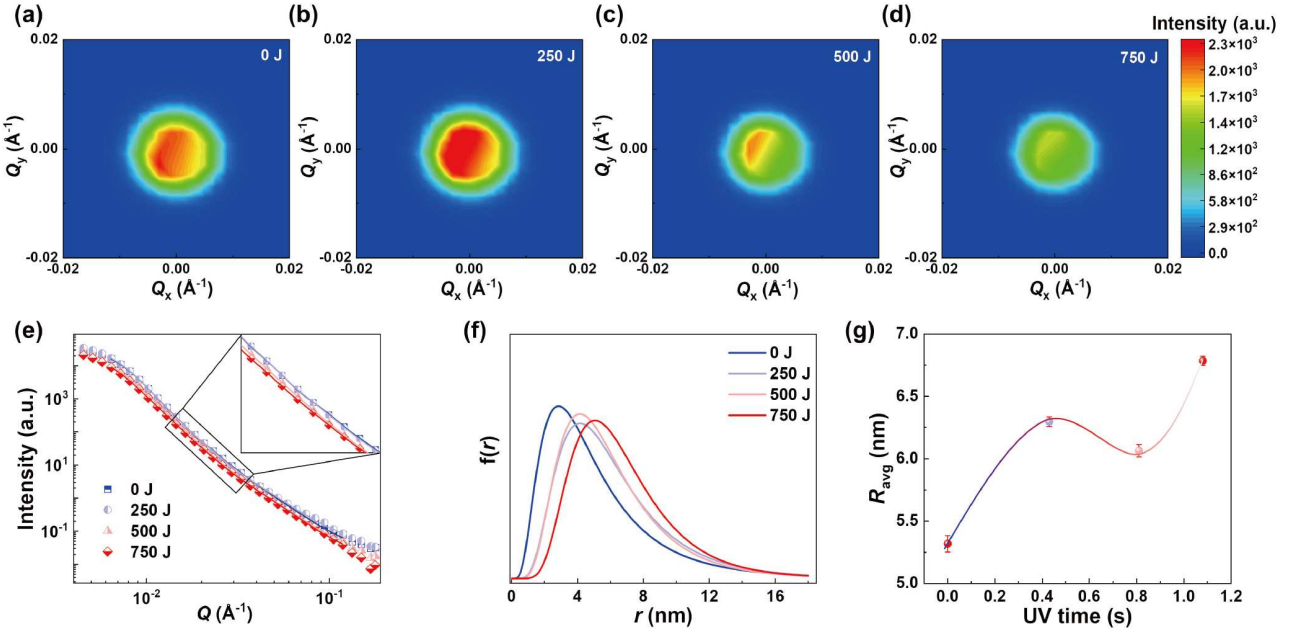

Figure 7 (Color online) 2D scattering patterns of 0 (a), 250 (b), 500 (c), and 750 (d) J APs. (e) Experimental SANS scattering profiles (point) and the fitted data (solid line) of 0, 250, 500, and 750 J APs, with the corresponding particle size distribution (f) and the evolution of mean particle radius R_{avg} (g).

above is primarily due to the reduction of the energy barrier for crystallization as a result of the UV-assisted high-energy state [85]. Additionally, the UV treatment also involves a transition of APs from a dense to loose atomic packing state [54], which effectively reduces the energy barrier required for atomic motions, and thereby a rapid mobility of atoms within the rejuvenated loosely packed glassy matrix during the crystallization process [99]. It accordingly leads to a decrease of thermal stability [100], e.g., the drop of T_x from 814 K of 0 J APs to 808 K of 750 J APs. As demonstrated in DSC (Figure 5(d)), once crystalline phases are incorporated in the glassy matrix, the free volume annihilates with a reduction of potential energy due to the locally densified process during structural ordering, which eventually impedes the degradation process of azo dyes for lowering the activity of APs catalysts. In addition to changes of the energy state [46], other factors, like the devastation of the passivation layer of 750 J APs, also affect the degradation behaviors. As depicted in Figure S11, the average particle size drops from (2.63 ± 2.03) μm of 500 J APs to (2.29 ± 1.32) μm of 750 J APs, and meanwhile some snowflake-like cracks on their surface. Only a minor fraction of 750 J APs displays flocculent characteristics, with a multi-level pore-like fluffy appearance (Figure S12), which promotes degradation reaction for exposing more active sites. More intriguingly, it is noticed that the surface morphology of 750 J APs remains more intact after degradation compared to the 500 J APs, which might be associated with its stronger anti-corrosion properties as discussed subsequently.

3.4 Electronic structure analyses

To monitor the evolution of the chemical bond and valence of APs during UV treatments, X-ray photoelectron spectroscopy (XPS) is performed, see Figure 8(a)-(g). The peak position of each ion and its content are listed in Table S6. Figure 8(a) and (b), obtained through XPS depth profiling, reveal that as etching depth and time increase, the O content sharply decreases from around 67 at.% to 46 at.% with the rising Fe content from 22 at.% to 39 at.%, further confirming that the commercial $Fe_{81}Si_9B_{10}$ APs consist of a thick oxide layer and an inner Fe-based amorphous core. The XPS survey spectra illustrate the existence of Fe, Si, B, and O elements in APs (Figure 8(c)). Herein, only Fe $2p_{3/2}$ peaks are

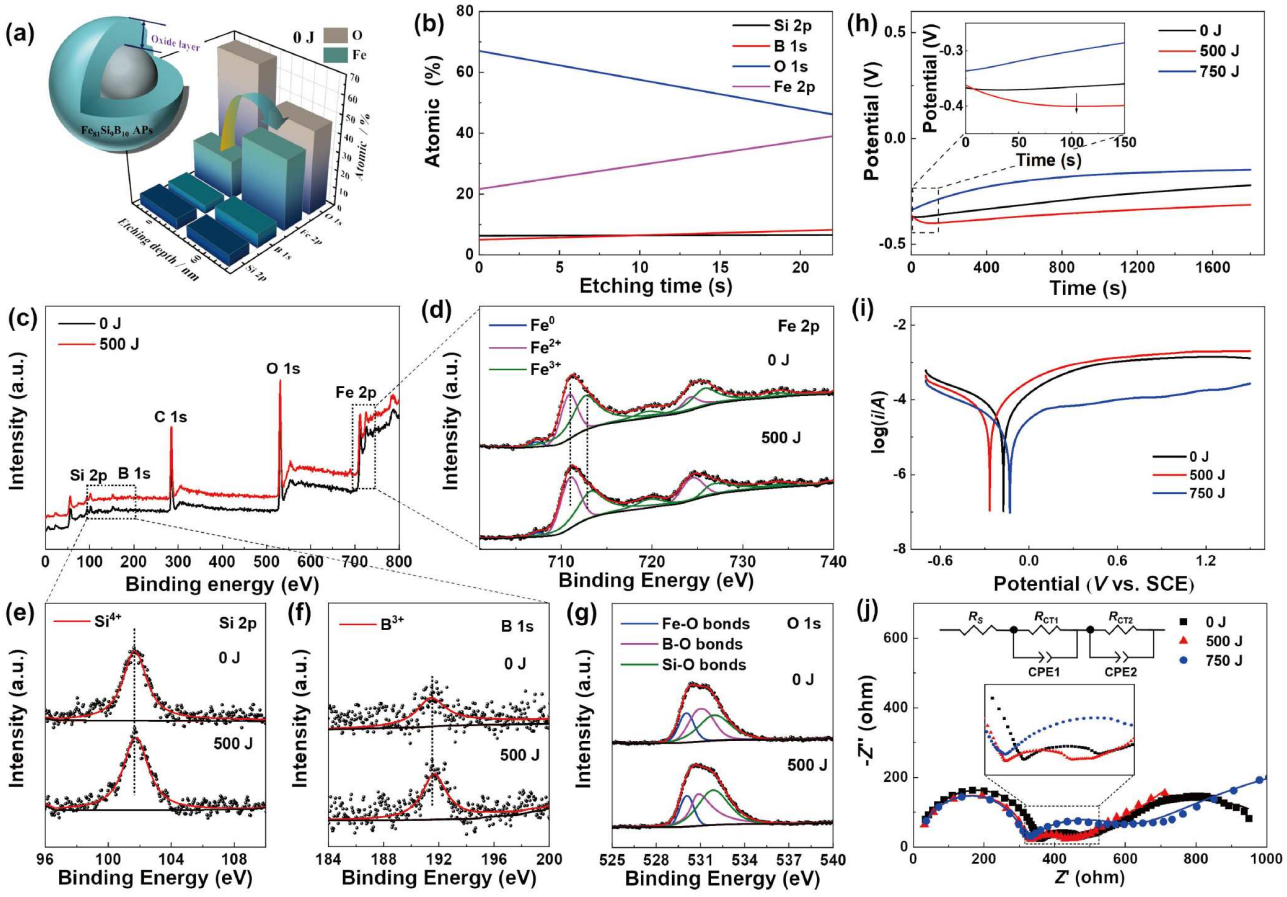

Figure 8 (Color online) (a, b) Elements distribution at the surface and within the interior of APs under a framework of core/shell structure. (c) High-resolution XPS survey spectra of 0 and 500 J APs, along with Fe 2*p* (d), Si 2*p* (e), B 1*s* (f), and O 1*s* (g). The OCP measurement (h), polarization curves (i), and EIS (j) of 0, 500, and 750 J APs, the inset in (j) shows the general fitted circuit.

analyzed for example, which can be divided into three peaks referring to Fe^0, Fe^{2+}, and Fe^{3+}, corresponding to 707.24 and 707.46 eV, 710.86 and 710.98 eV, and 712.64 and 713.21 eV for 0 and 500 J APs, respectively (Figure 8(d)). Besides, the oxidized Si^{4+} (101.63, 101.68 eV) and B^{3+} (191.43, 191.68 eV) coexist in 0 and 500 J samples, respectively (Figure 8(e) and (f)). It is found that the binding energies of Fe 2*p*, B 1*s*, and Si 2*p* slightly shift to higher positions after UV, indicating the occurrence of a more significant oxidation reaction (Table S6). The peaks of O 1*s* indicate the appearance of some iron oxides (e.g., FeO_x, Fe_2O_3, and FeOOH), SiO_2, and B_2O_3 on the surface of $Fe_{81}Si_9B_{10}$ APs [62] (Figure 8(g)). It is worth noting that more B–O tends to form a loose oxide film on the powder surface under UV at high energy. The thicker oxide layer formed during UV, although easily peelable, hinders the detection of Fe [101]. It well explains much lower content of Fe in UV-treated APs, especially 500 J APs, as demonstrated by both EDS and XPS as compared with the as-cast one. After degradation, the characteristic peak at Fe^0 disappears, indicating that Fe^0 in the amorphous matrix has oxidized as an electron provider during the degradation of the azo dye (Figure S13). The total amount of Fe on the surface of the powders after the degradation reaction (0 and 500 J) is much lower than that on the surface of the powders before the degradation reaction (Table S6), verifying that Fe is involved in the degradation of MB [75]. Furthermore, as shown in Figure 8(d) and Table S6, 500 J APs possess a relatively high content of Fe^{2+}, which facilitates the Fenton-like reaction due to the generation of ·OH that originates from the reaction of Fe^{2+} with H_2O_2.

Figure 8(h) depicts the changes in surface stability of the samples under acidic conditions, as illustrated by the OCP. The noble potentials of APs, except for the 750 J sample initially shift to a lower position, implying a gradual dissolution of the native oxide layer. Subsequently, positive changes are observed in all three samples at the later stage, which is attributed to the cathodic process involved in the formation of a passivating film. Notably, 500 J APs exhibit a lower OCP potential, suggesting a poorer surface stability and a greater corrosion tendency, which is further confirmed by its most negative corrosion potential (-0.265 V_{SCE}) (Figure 8(h) and Table S7) [69,102]. The weak corrosion resistance of 500 J APs, coincides with the observed surface damage in Figure 4(f)-(h), which facilitates surface reactivation and thereby promotes the degradation reaction.

Furthermore, the EIS spectra with frequencies ranging from 0.01 Hz to 1000 kHz for these samples are displayed in Figure 8(i). Compared with 0 J APs, both 500 and 750 J APs show a smaller first semicircle with the passivated film impedance [103]. Especially for the 500 J sample, it exhibits the smallest secondary semicircle, indicating low electron transfer impedance, which agrees with its highest catalytic activity as shown in Figure 1. Whereas, 750 J APs under longer UV processing time show a more intact surface (Figure S12), corresponding to a pronounced corrosion resistance with the shift of OCP and corrosion potential (-0.129 V_{SCE}) to the most positive positions as well as the largest second semicircle among three AP samples, see Figure 8(h)-(j). The inset in Figure 8(j) demonstrates the simplified equivalent circuit for the EIS data fitting; the corresponding results are summarized in Table S8. The strong anti-corrosion of 750 J APs might be attributed to the annihilation of free volumes due to the structural relaxation, as demonstrated in DSC traces in Figure 5(d), coinciding with the reduction of the average atomic distance (Figure 5(a)). It will lead to the formation of a highly protective passive film, which effectively lowers the energy state of the surface and results in the slow dissolution rate of atoms as reported by Zhang et al. [102].

3.5 Degradation mechanism

Undoubtedly, it is necessary to comprehend the degradation mechanism of catalysts via the analysis of surface morphology and valence states due to the surface-mediated process of the Fenton-like reaction. These APs consist of a shell structure formed by a surface oxide layer and an inner core (Figure 8(a)). As shown in Figure 9(a), the disruption of the oxide layer exposes fresh surfaces (amorphous zero-valent iron), which significantly accelerates the Fe^{2+}/Fe^{3+} redox circulation. Furthermore, abundant protrusions on the surface effectively enhance reaction rates by boosting reactive sites and forming clear transport pathways. Whereas, with increasing UV processing time, such protrusions diminish, along with the emergence of a broken oxide layer. The UV-induced fragmentation and welding [78] of powder particles, consequently, leads to a large reaction surface area. However, these explanations do not fully account for the observed changing trends in degradation performances; we need to seek more evidence from both atomic and electronic configurational perspectives to clarify the underlying physical mechanism for dye degradation by utilizing metastable amorphous materials as catalysts.

To conveniently interpret the complex physical phenomenon of amorphous materials, PEL theory was developed by Debenedetti and Stillinger [86], which stems from a fundamental concept that the properties of condensed matter are determined by the interaction between constituent atoms. As shown in Figure 9(b), there are many local energy minima (or basins) on the PEL diagram, representing different metastable states of disordered configurations. Based on the PEL theory, the variation of properties during deformation, structural relaxation/aging [104], glass transition, etc., in amorphous materials is strongly associated with the atomic hopping between neighboring basins by overcoming energy barriers. For the as-cast sample, its XRD and DSC results

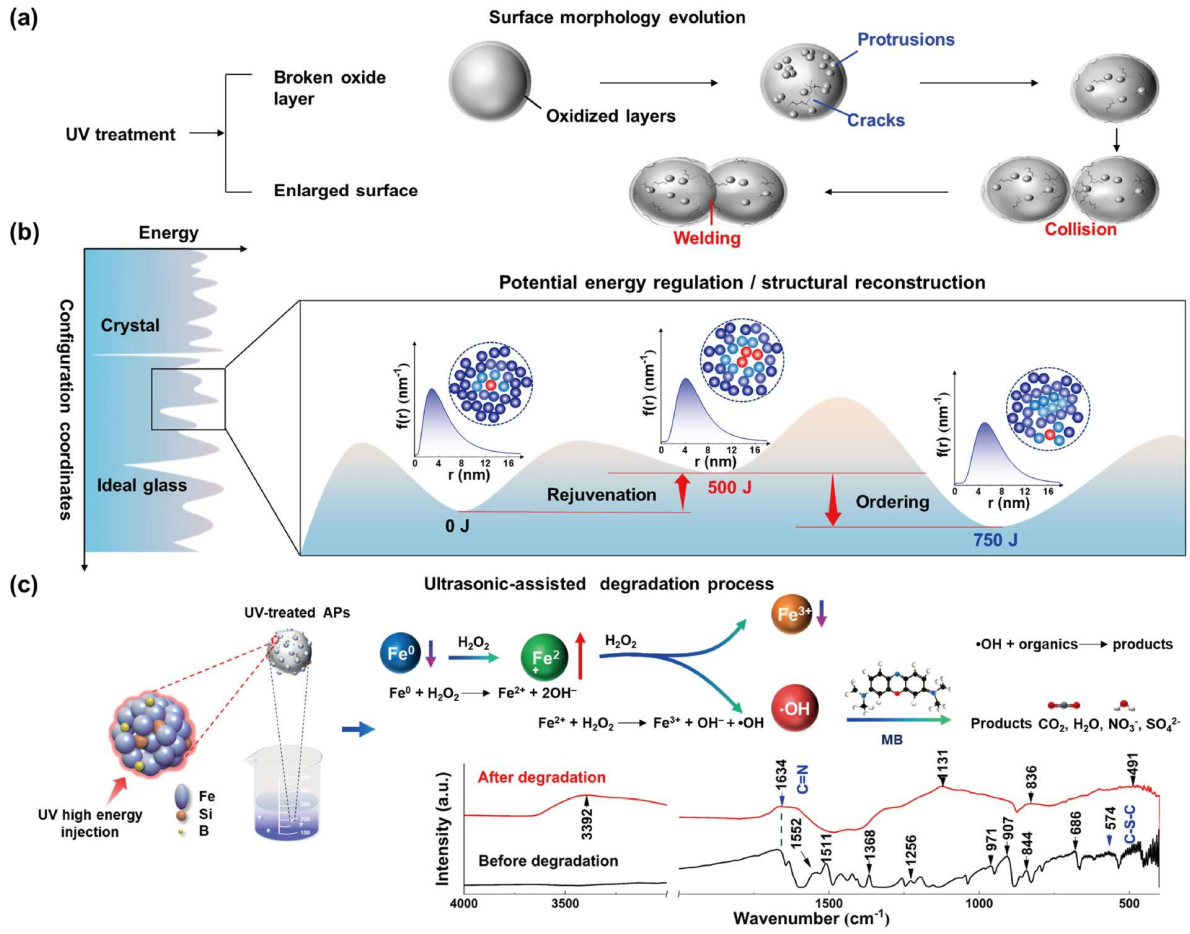

Figure 9 (Color online) Schematic diagram of UV-induced degradation mechanism from viewpoints of microstructure, surface morphology evolution, and potential energy regulation. (a) Evolution of the surface morphology of APs under UV. (b) The PEL image of UV-treated APs. (c) A schematic of the degradation process following the main three steps with decreased contents of Fe^0 and Fe^{3+} and an increment of Fe^{2+}, along with the representative particle surface morphology of 500 J APs before degradation. The infrared spectra of 500 J APs were plotted to show products after degradation, and key peaks before degradation include: 1634 cm^{-1} for C=N central ring stretching, 1552 and 1511 cm^{-1} for C=C, 1368 cm^{-1} for multiple ring stretching, 1256, 971, 907, 844, 686 cm^{-1} for C–H bonds, 574 cm^{-1} for C–S–C skeleton vibration; the peaks after degradation include: 3392 cm^{-1} for O–H, 1131, 491 cm^{-1} for C–O, and 836 cm^{-1} for C–H.

show a broad amorphous hump, a high T_x of 814 K, as well as a modest ΔH_{rel} of 1.837 kJ mol^{-1} among the studied samples, indicating a relatively stable state. Thus, the system is located at a low energy position on the PEL diagram. In fact, the system can jump into a higher energy state by post processes through the energy injection during mechanical deformation, like UV treatments, which is so-called rejuvenation [105,106]. Here, we find a significant increase of ΔH_{rel} to 2.169 kJ mol^{-1} in 500 J APs upon the UV treatment, which suggests that the sample reaches a high-energy rejuvenated state. It results in the system residing in a higher position on the PEL diagram with surrounding low energy barriers, which is consistent with the low E_a of 45.32 kJ mol^{-1} during degradation for 500 J APs. Nevertheless, further increasing UV energy does not intensify the structural rejuvenation. A pronounced reduction of ΔH_{rel} from 2.169 to 0.635 kJ mol^{-1} occurs in 750 J APs, indicating an atomic configurational transition from a metastable to a more stable equilibrium state locally due to the ultrasonic-induced structural relaxation/aging. Accordingly, 750 J APs lie in another basin on the PEL diagram with a lower potential energy, thus the corresponding atomic rearrangement needs overcoming a higher energy barrier, which is consistent with its higher E_a of 94.28 kJ mol^{-1}. Therefore, the degradation efficiency of 750 J APs is much lower than that of 500 J APs.

In addition to the perspective of PEL theory for elaborating the UV-induced degradation mechanism, the structural reconstruction of APs also influences their catalytic performances, which primarily originates from changes in short-range atomic configurations. Previous studies show that the participation of the α-Fe crystalline phase in $Fe_{78}Si_9B_{13}$ amorphous alloys could obviously reduce the catalytic activity during degradation, attributed to the strong atomic bonding of ordered configurations that are hard to break up [41]. In this work, 0 and 500 J APs retain an amorphous

nature with no significant crystalline phase. Whereas, it has been reported that the packing state of systems can be effectively manipulated via the UV treatment [76]. The structural order estimated by HRTEM demonstrates the more disordered atomic configurations of the 500 J APs. The increased repulsion (λ = 200.39) inside SRO also promotes structural disordering of the 500 J APs, as evidenced by UV-induced elevation of free volume that drives loosely atomic packing and weak atomic bonding within the amorphous matrix. These randomly distributed MRO disordered configurations can be indicated by SANS as well (Figure 7), which are easier to activate and consequently improve catalytic performances. This structural reconstruction at both SRO and MRO scales, combined with the energy regulation as demonstrated in Figure 9(b), coincides with the electrochemical analysis that the 500 J sample exhibits a high charge transfer rate as shown by the smallest secondary semicircle in the EIS spectra. In contrast, some nanocrystals such as α-Fe and FeSi with a high thermal stability are precipitated in 750 J APs, accompanied by a high degree of order, and a low value of ΔH_{rel} (0.635 kJ mol^{-1}) and λ (194.98), implying the annihilation of free volume during the UV treatment with longer time. These ordered configurations often show strong chemical bonding and dense atomic packing, which impedes charge transfer (see Figure 8(j)) and eventually causes the reduction of the degradation efficiency.

Based on the above analysis, the efficient degradation process of azo dyes by utilizing the UV-treated $Fe_{81}Si_9B_{10}$ APs as a catalyst can be illustrated as follows (Figure 9(c)). The degradation reaction in the MB dye solution is promoted by cracking and shedding of the surface oxide layer (Figure 9(a)) from the amorphous matrix of $Fe_{81}Si_9B_{10}$ APs during the high-energy UV treatment. The invasion of high-concentration H^+ on the surface facilitates the formation of effective mass transport pathways, which enables continuous Fenton-like reactions between ZVI and the dye solution. This process benefits from the high-energy disordered state and weak bonding characteristics of the UV-treated APs. It readily overcomes the energy barriers of degradation reaction and promotes charge transfer between Fe^0 and iron oxides (Fe^{2+} and Fe^{3+}), in which Fe^0 is consumed as an electron donor to directly generate Fe^{2+}, and meanwhile forcing Fe^{3+} to be reduced to Fe^{2+} ($2Fe^{3+} + Fe^0 \rightarrow 3Fe^{2+}$) [107], thereby resulting in a significant rise of Fe^{2+} content during degradation with decreasing Fe^0 and Fe^{3+} contents after the UV treatment (see XPS spectra analyses in Figure 8, Figure S13 and Table S6). In this way, the high content of Fe^{2+} accelerates the production of ·OH, which effectively facilitates the degradation of MB into non-toxic carbon dioxide (CO_2), water, and other small species, as evidenced by the breakage of the aromatic ring of the MB dye, e.g., the C=N central ring stretching at 1634 cm^{-1}, skeleton vibration C–S–C at 574 cm^{-1}, see the Fourier transform infrared spectroscopy at the bottom of Figure 9(c) (more details can be found in Figure S14).

Although crystallization has a side effect on degradation performances as shown in this work, some studies point out that the galvanic cell effect between the amorphous matrix and nanocrystals may promote degradation reaction [43,45,108]. Therefore, the energy state, structural order, chemical bond and valence, and degradation properties in amorphous materials subjected to UV might require further studies, especially at high UV energy or frequencies.

4 Conclusions

In conclusion, a comprehensive study based on HRTEM, high-energy XRD, SANS, etc., is conducted to elaborate on the effect of the UV treatment on the degradation performances of $Fe_{81}Si_9B_{10}$ APs. The 500 J APs show the highest degradation efficiency due to a high k_{obs} and low E_{a} even at a low dosage of only one-fifth of the normally used dosage (0.1 g L^{-1}), which is attributed to the UV-assistant structural reconstruction at both SRO and MRO accompanied by the devastation of the passivation layer. The fast charge transfer rate, a substantial reactive surface area, and a stimulated loose packing state with weakened atomic bonding and high potential energy synergistically contribute to the high degradation efficiency of the UV-treated APs. However, excessive UV energy leads to an ordering process with structural relaxation/aging and thereby crystallization, which eventually lowers the degradation effectiveness of APs. This work provides a deep insight into the UV-assistant degradation mechanism from perspectives of the energy state, order, atomistic and electronic structure modulation, which might inspire a new view on the degradation mechanism of the high-efficient amorphous catalysts achieved via other post-processing techniques such as annealing [43-45], dealloying [46,47], electrochemical etching [48], pulsed laser micromachining [49], etc.

This work was supported by the National Natural Science Foundation of China (Grant Nos. 52071078, and 52401201), the "Zhishan" Scholars Programs of Southeast University (Grant No. 2242021R41158), and the Jiangsu Key Laboratory for Advanced Metallic Materials (Grant No. BM2007204). This research work is supported by the Big Data Computing Center of Southeast University. We thank the staff members of the Small Angle Neutron Scattering (https://csns.cn/31113.02.CSNS.SANS) at the China Spallation Neutron Source (CSNS) (https://csns.cn/31113.02.CSNS) for providing technical support and assistance in data collection and analysis.

Conflict of interest The authors declare that they have no conflict of interest.

Supporting Information

The supporting information is available online at http://phys.scichina.com and https://link.springer.com. The supporting materials are published as submitted, without typesetting or editing. The responsibility for scientific

accuracy and content remains entirely with the authors.

1 S. Khandaker, M. M. Bashar, A. Islam, M. T. Hossain, S. H. Teo, and M. R. Awual, Renew. Sustain. Energy Rev. **157**, 112051 (2022).
2 Saakshy, A. K. Sharma, R. K. Jain, R. K. Jain. in *Biotechnology for Environmental Management and Resource Recovery*, edited by R.C. Kuhad, and A. Singh (Springer, Heidelberg, 2013), pp. 279–288.
3 C. Ramos-Souza, D. H. Bandoni, A. P. A. Bragotto, and V. V. De Rosso, Comp. Rev. Food. Sci. Food Saf. **22**, 380 (2023).
4 F. Rafii, J. D. Hall, and C. E. Cerniglia, Food Chem. Toxicol. **35**, 897 (1997).
5 É. Hansen, P. Monteiro de Aquim, and M. Gutterres, J. Environ. Manage. **294**, 113003 (2021).
6 Z. Yao, Y. Chen, X. Wang, K. Hu, S. Ren, J. Zhang, Z. Song, N. Ren, and X. Duan, Nat. Commun. **16**, 148 (2025).
7 X. Shi, Y. Jiang, B. Zeng, Z. Sun, M. Yun, P. Lv, Y. Jia, and X. Zheng, Nat. Catal. **8**, 67 (2025).
8 A. Tkaczyk, K. Mitrowska, and A. Posyniak, Sci. Total Environ. **717**, 137222 (2020).
9 B. Antizar-ladislao, J. Lopez-real, and A. Beck, Crit. Rev. Environ. Sci. Tech. **34**, 249 (2004).
10 R. Al-Tohamy, S. S. Ali, F. Li, K. M. Okasha, Y. A. G. Mahmoud, T. Elsamahy, H. Jiao, Y. Fu, and J. Sun, Ecotoxicol. Environ. Saf. **231**, 113160 (2022).
11 X. Wang, C. Jiang, B. Hou, Y. Wang, C. Hao, and J. Wu, Chemosphere **206**, 587 (2018).
12 L. Sun, Y. Mo, and L. Zhang, Chemosphere **294**, 133801 (2022).
13 V. Katheresan, J. Kansedo, and S. Y. Lau, J. Environ. Chem. Eng. **6**, 4676 (2018).
14 D. Rawat, R. S. Sharma, S. Karmakar, L. S. Arora, and V. Mishra, Ecotoxicol. Environ. Saf. **148**, 528 (2018).
15 S. Varjani, P. Rakholiya, H. Y. Ng, S. You, and J. A. Teixeira, Bioresour. Tech. **314**, 123728 (2020).
16 P. V. Nidheesh, R. Gandhimathi, and S. T. Ramesh, Environ. Sci. Pollut. Res. **20**, 2099 (2013).
17 M. Saeed, M. Muneer, A. Haq, and N. Akram, Environ. Sci. Pollut. Res. **29**, 293 (2022).
18 S. Nam, and P. G. Tratnyek, Water Res. **34**, 1837 (2000).
19 A. Iqbal, A. Yusaf, M. Usman, T. Hussain Bokhari, and A. Mansha, Int. J. Environ. Anal. Chem. **104**, 5503 (2024).
20 L. C. Zhang, Z. Jia, F. Lyu, S. X. Liang, and J. Lu, Prog. Mater. Sci. **105**, 100576 (2019).
21 J. Guo, G. Song, X. Zhang, and M. Zhou, Environ. Sci.-Water Res. Technol. **9**, 2429 (2023).
22 M. Cheng, C. Lai, Y. Liu, G. Zeng, D. Huang, C. Zhang, L. Qin, L. Hu, C. Zhou, and W. Xiong, Coord. Chem. Rev. **368**, 80 (2018).
23 Y. Tian, W. Fu, Q. Wang, Y. Tang, and M. Zhou, Chem. Eng. J. **427**, 131694 (2022).
24 C. Zhang, Z. Zhu, H. Zhang, and Z. Hu, J. Non-Cryst. Solids **358**, 61 (2012).
25 C. Q. Zhang, Z. W. Zhu, H. F. Zhang, and Z. Q. Hu, Chin. Sci. Bull. **56**, 3988 (2011).
26 J. Wang, Y. Liu, M. Chen, G. Xie, D. V. Louzguine‐Luzgin, A. Inoue, and J. H. Perepezko, Adv. Funct. Mater. **22**, 2567 (2012).
27 Y. Tang, Y. Shao, N. Chen, X. Liu, S. Q. Chen, and K. F. Yao, RSC Adv. **5**, 34032 (2015).
28 P. Duwez, and S. C. H. Lin, J. Appl. Phys. **38**, 4096 (1967).
29 A. Inoue, Y. Shinohara, and J. S. Gook, Mater. Trans. JIM **36**, 1427 (1995).
30 Y. Yoshizawa, S. Oguma, and K. Yamauchi, J. Appl. Phys. **64**, 6044 (1988).
31 Y. Chen, X. Tong, Y. Cai, Y. Wang, M. Gao, H. Ke, G. Zhang, H. Bai, W. Wang, J. Huo, et al., Sci. China-Phys. Mech. Astron. **68**, 276111 (2025).
32 C. Zhao, C. Dun, Q. Man, and B. Shen, Intermetallics **32**, 408 (2013).
33 W. H. Wang, Prog. Mater. Sci. **57**, 487 (2012).
34 D. D. Coimbrão, G. Zepon, G. Y. Koga, D. A. Godoy Pérez, F. H. Paes de Almeida, V. Roche, J. C. Lepretre, A. M. Jorge Jr., C. S. Kiminami, C. Bolfarini, et al., J. Alloys Compd. **826**, 154123 (2020).
35 S. Chen, M. Li, Q. Ji, T. Feng, S. Lan, and K. F. Yao, J. Mater. Sci. Tech. **117**, 49 (2022).
36 Z. Deng, X. H. Zhang, K. C. Chan, L. Liu, and T. Li, Chemosphere **174**, 76 (2017).
37 H. X. Li, Z. C. Lu, S. L. Wang, Y. Wu, and Z. P. Lu, Prog. Mater. Sci. **103**, 235 (2019).
38 C. Zhang, H. Zhang, M. Lv, and Z. Hu, J. Non-Cryst. Solids **356**, 1703 (2010).
39 C. Zhang, Z. Zhu, H. Zhang, and Z. Hu, J. Environ. Sci. **24**, 1021 (2012).
40 X. Wang, Y. Pan, Z. Zhu, and J. Wu, Chemosphere **117**, 638 (2014).
41 Z. Jia, X. Duan, P. Qin, W. Zhang, W. Wang, C. Yang, H. Sun, S. Wang, and L. Zhang, Adv. Funct. Mater. **27**, 1702258 (2017).
42 L. Zhang, and S. Liang, Chem. Asian J. **13**, 3575 (2018).
43 S. Chen, N. Chen, M. Cheng, S. Luo, Y. Shao, and K. Yao, Intermetallics **90**, 30 (2017).
44 Q. Chen, Z. Qi, Y. Feng, H. Liu, Z. Wang, L. Zhang, and W. Wang, J. Non-Cryst. Solids **598**, 121952 (2022).
45 S. Chen, G. Yang, S. Luo, S. Yin, J. Jia, Z. Li, S. Gao, Y. Shao, and K. Yao, J. Mater. Chem. A **5**, 14230 (2017).
46 S. Q. Chen, M. Li, Q. Ji, X. Chen, S. Lan, T. Feng, and K. F. Yao, J. Non-Cryst. Solids **571**, 121070 (2021).
47 Q. Chen, L. Guo, H. Di, Z. Qi, Z. Wang, Z. Song, L. Zhang, L. Hu, and W. Wang, Adv. Sci. **10**, 2304045 (2023).
48 Q. Zhang, S. X. Liang, Z. Jia, W. Zhang, W. Wang, and L. C. Zhang, J. Mater. Sci. Tech. **61**, 159 (2021).
49 Q. Chen, H. Di, Z. Qi, Z. Wang, Z. Song, L. C. Zhang, L. Guo, and W. Wang, J. Mater. Sci. Tech. **188**, 191 (2024).
50 Z. Li, X. Li, Z. Huang, Z. Zhang, X. Liang, H. Liu, P. K. Liaw, J. Ma, and J. Shen, Acta Mater. **225**, 117569 (2022).
51 L. Li, X. Li, Z. Huang, J. Huang, Z. Liu, J. Fu, W. Wen, Y. Zhang, S. Huang, S. Ren, et al., Nat. Commun. **14**, 6305 (2023).
52 Z. Chen, S. Ren, R. Zhao, J. Zhu, X. Li, H. Zhang, H. Lin, J. Zhu, S. Sohrabi, W. Ruan, et al., J. Mater. Sci. Tech. **181**, 231 (2024).
53 W. Li, C. Wang, L. Y. Li, C. Zhang, J. Ma, X. K. Xi, K. Tao, J. C. Qiao, C. C. Yuan, and W. H. Wang, Int. J. Mech. Sci. **287**, 109960 (2025).
54 K. Wu, Y. Meng, X. Li, J. Ma, P. Zhang, W. Li, L. Huo, and H. J. Lin, Intermetallics **125**, 106820 (2020).
55 Z. Lv, Y. Yan, C. Yuan, B. Huang, C. Yang, J. Ma, J. Wang, L. Huo, Z. Cui, X. Wang, et al., Mater. Des. **194**, 108876 (2020).
56 F. J. Liu, K. F. Yao, and H. Y. Ding, Intermetallics **19**, 1674 (2011).
57 C. Gao, S. Chen, X. Quan, H. Yu, and Y. Zhang, J. Catal. **356**, 125 (2017).
58 Y. Zhang, J. Gou, T. Yang, Y. Ke, and T. Ma, Acta Mater. **244**, 118548 (2023).
59 X. Wu, S. Lan, X. Li, M. Yang, Z. Wu, X. Wei, H. He, M. Naeem, J. Zhou, Z. Lu, et al., J. Mater. Sci. Tech. **101**, 285 (2022).
60 X. Wu, X. Li, Z. Wu, X. L. Wang, X. Wei, J. Zhou, Z. Lu, E. P. Gilbert, Z. Sun, J. Ding, et al., J. Miner. Met. Mater. Soc. **76**, 6917 (2024).
61 I. Khan, K. Saeed, I. Zekker, B. Zhang, A. H. Hendi, A. Ahmad, S. Ahmad, N. Zada, H. Ahmad, L. A. Shah, et al., Water **14**, 242 (2022).
62 J. H. Sun, S. P. Sun, J. Y. Sun, R. X. Sun, L. P. Qiao, H. Q. Guo, and M. H. Fan, Ultrason. Sonochem. **14**, 761 (2007).
63 X. Tao, Q. Chen, L. Ji, and G. Huang, J. Non-Cryst. Solids **570**, 121010 (2021).
64 J. Chen, and L. Zhu, Catal. Today **126**, 463 (2007).
65 C. Li, W. Zhai, L. Tian, Y. Lu, J. Zhai, Y. Wang, X. Li, and S. Kou, Phys. Stat. Solidi (a) **220**, 2300297 (2023).
66 S. X. Liang, W. Zhang, W. Wang, G. Jia, W. Yang, and L. C. Zhang, J. Phys. Chem. Solids **132**, 89 (2019).
67 W. H. Luo, Q. J. Chen, L. Ji, X. Y. Peng, G. S. Huang. J. Rare Earths **40**, 605 (2025).
68 L. Hou, Q. Wang, X. Fan, F. Miao, W. Yang, and B. Shen, New J.

Chem. **43**, 6126 (2019).
69 Z. Jia, J. Kang, W. C. Zhang, W. M. Wang, C. Yang, H. Sun, D. Habibi, and L. C. Zhang, Appl. Catal. B-Environ. **204**, 537 (2017).
70 S. Liang, Z. Jia, Y. Liu, W. Zhang, W. Wang, J. Lu, and L. Zhang, Adv. Mater. **30**, 1802764 (2018).
71 W. Yang, Q. Wang, W. Li, L. Xue, H. Liu, J. Zhou, J. Mo, and B. Shen, Mater. Des. **161**, 136 (2019).
72 Q. Chen, Z. Yan, H. Zhang, L. C. Zhang, H. Ma, W. Wang, and W. Wang, Materials **13**, 3694 (2020).
73 Y. Ma, L. Xie, Q. Li, C. Chang, H. Li, B. Mu, and X. Ma, J. Phys. Chem. Solids **163**, 110596 (2022).
74 Z. Qi, G. Li, Q. Chen, Z. Yan, H. Zhang, Y. Feng, H. Liu, X. Li, and W. Wang, J. Non-Cryst. Solids **576**, 121275 (2022).
75 Q. Wang, M. Chen, P. Lin, Z. Cui, C. Chu, and B. Shen, J. Mater. Chem. A **6**, 10686 (2018).
76 Z. Jia, X. Duan, W. Zhang, W. Wang, H. Sun, S. Wang, and L. C. Zhang, Sci. Rep. **6**, 38520 (2016).
77 S. Q. Chen, Y. Shao, M. T. Cheng, and K. F. Yao, J. Non-Cryst. Solids **473**, 74 (2017).
78 F. Ning, and W. Cong, J. Manuf. Process. **51**, 174 (2020).
79 X. Peng, J. Han, Y. Wang, Z. Bo, A. Nie, P. Li, Y. Li, H. Wu, P. Liu, Z. Lu, et al., Appl. Mater. Today **29**, 101689 (2022).
80 H. Lou, Z. Zeng, F. Zhang, S. Chen, P. Luo, X. Chen, Y. Ren, V. B. Prakapenka, C. Prescher, X. Zuo, et al., Nat. Commun. **11**, 314 (2020).
81 F. Spieckermann, D. Şopu, V. Soprunyuk, M. B. Kerber, J. Bednarčík, A. Schökel, A. Rezvan, S. Ketov, B. Sarac, E. Schafler, et al., Nat. Commun. **13**, 127 (2022).
82 J. Krausser, K. H. Samwer, and A. Zaccone, Proc. Natl. Acad. Sci. USA **112**, 13762 (2015).
83 C. C. Yuan, J. Ma, and X. K. Xi, Mater. Sci. Eng.-A **532**, 430 (2012).
84 A. Slipenyuk, and J. Eckert, Scripta Mater. **50**, 39 (2004).
85 C. C. Yuan, Z. W. Lv, X. Li, C. M. Pang, R. Liu, C. Yang, J. Ma, W. W. Zhu, B. Huang, and H. B. Ke, Intermetallics **153**, 107803 (2023).
86 P. G. Debenedetti, and F. H. Stillinger, Nature **410**, 259 (2001).
87 Q. Hao, G. Xing, E. Pineda, C. Fusco, L. Chazeau, J. M. Pelletier, Y. Wang, Y. Yang, and J. Qiao, Sci. China-Phys. Mech. Astron. **68**, 234611 (2025).
88 Z. Wang, F. Yang, A. Bernasconi, K. Samwer, and A. Meyer, Phys. Rev. B **98**, 024204 (2018).
89 J. Yu, Y. Lou, Z. Wang, L. Yang, G. Huang, and J. Ma, J. Non-Cryst. Solids **629**, 122875 (2024).
90 Y. Zhang, H. Zhao, Y. Q. Yan, X. Tong, J. Ma, H. B. Ke, and W. H. Wang, J. Non-Cryst. Solids **597**, 121894 (2022).
91 R. Babilas, Mater. Charact. **107**, 7 (2015).
92 X. J. Liu, G. L. Chen, H. Y. Hou, X. Hui, K. F. Yao, Z. P. Lu, and C. T. Liu, Acta Mater. **56**, 2760 (2008).
93 S. Fu, G. Chen, H. Guo, S. Liu, M. Yan, Y. Lou, H. Ying, Z. Yao, Y. Ren, W. Jiang, et al., Small **19**, 2300721 (2023).
94 B. Sarac, C. Gammer, L. Deng, E. Park, Y. Yokoyama, M. Stoica, and J. Eckert, Nanoscale **10**, 1081 (2018).
95 S. J. Kang, Q. P. Cao, J. Liu, Y. Tang, X. D. Wang, D. X. Zhang, I. S. Ahn, A. Caron, and J. Z. Jiang, J. Alloys Compd. **795**, 493 (2019).
96 C. C. Yuan, C. Deng, H. P. Zhang, M. Z. Li, and B. L. Shen, Intermetallics **112**, 106501 (2019).
97 C. C. Yuan, F. Yang, X. K. Xi, C. L. Shi, D. Holland-Moritz, M. Z. Li, F. Hu, B. L. Shen, X. L. Wang, A. Meyer, et al., Mater. Today **32**, 26 (2020).
98 C. C. Yuan, F. Yang, F. Kargl, D. Holland-Moritz, M. Z. Li, X. L. Wang, B. Zhang, W. H. Wang, and A. Meyer, Acta Mater. **285**, 120652 (2025).
99 J. Pan, F. Duan. Acta Metall. Sin. **57**, 439 (2021).
100 F. Chu, B. Han, K. Edalati, J. Ma, Y. Meng, C. Wang, F. Yang, P. Zhang, and H. J. Lin, Scripta Mater. **204**, 114145 (2021).
101 B. Wei, X. Li, H. Sun, K. Song, and L. Wang, J. Non-Cryst. Solids **575**, 121212 (2022).
102 L. M. Zhang, S. D. Zhang, A. L. Ma, H. X. Hu, Y. G. Zheng, B. J. Yang, and J. Q. Wang, Corros. Sci. **144**, 172 (2018).
103 J. Song, J. Power Sour. **111**, 255 (2002).
104 Z. Y. Zhou, Q. Yang, and H. B. Yu, Prog. Mater. Sci. **145**, 101311 (2024).
105 H. Zhao, F. Sun, X. Li, Y. Ding, Y. Q. Yan, X. Tong, J. Ma, H. B. Ke, and W. H. Wang, Scripta Mater. **194**, 113606 (2021).
106 Y. Du, Q. Zhou, S. Li, D. Hua, X. Pei, H. Wang, W. Zhou, and W. Liu, Adv. Funct. Mater. **35**, e07634 (2025).
107 A. Lassoued, L. J. Liu, and J. F. Li, J. Mater. Sci. **57**, 2039 (2022).
108 P. P. Wang, J. Q. Wang, J. T. Huo, W. Xu, X. M. Wang, and G. Wang, Sci. China-Phys. Mech. Astron. **60**, 076112 (2017).